metals

MDPI

Article

Inhibition Mechanism of Crevice Corrosion for 304 Stainless Steel by Intermittent Anodic Polarization in Natural Seawater

Guowei Wu [1], Guo Zheng [1], Guanwen Zheng [1], Shuo Yang [2,3] and Peichang Deng [2,3,*]

[1] Zhanjiang Power Co., Ltd., Zhanjiang 524099, China
[2] College of Chemistry and Environment, Guangdong Ocean University, Zhanjiang 524088, China
[3] Zhanjiang Key Laboratory of Corrosion and Protection for Ocean Engineering and Equipment, Zhanjiang 524088, China
* Correspondence: dpc0520@163.com; Tel.: +86-151-1358-6218

Abstract

Marine engineering components of 304 stainless steel inevitably form crevice structures in service, which readily trigger severe crevice corrosion in seawater. Conventional protection strategies, including cathodic protection, organic coatings and corrosion inhibitors, show evident limitations within occluded crevices because of IR drop and mass transfer barriers. In this work, a 10 × 10 array electrode was employed to construct a simulated crevice device with a 0.3 mm gap width. Static immersion tests were carried out in natural seawater collected from Zhanjiang Bay for 75 days, using a blank group and an intermittent anodic polarization group (0.1 V vs. SCE applied for 10 min every 30 min; three independent specimens per group). In situ galvanic potential/current distribution mapping, electrochemical impedance spectroscopy (EIS) and ultra-depth-of-field microscopic observations were performed. Stable oxygen concentration cells were gradually built inside the crevices of blank specimens, producing band-shaped heterogeneous galvanic signals and massive pitting initiation. Intermittent anodic polarization homogenized the crevice internal potential distribution, reduced the galvanic current magnitude and effectively repaired the passive films: the inner crevice film resistance increased from 2.62×10^6 Ω·cm^2 to 2.59×10^7 Ω·cm^2, and the pitting density decreased markedly. Intermittent anodic polarization ameliorates the occluded electrochemical environment and mitigates crevice corrosion of 304 stainless steel in seawater, offering a potential supplementary strategy for marine stainless-steel components with crevice structures.

Keywords: 304 stainless steel; natural seawater; crevice corrosion; intermittent anodic polarization; array electrode; passive film; localized corrosion

Check for updates

Academic Editor: Petros E. Tsakiridis

Received: 2 October 2026
Revised: 21 October 2026
Accepted: 27 October 2026
Published: 10 November 2026

Copyright: © 2026 by the authors. Licensee MDPI, Basel, Switzerland. This article is an open access article distributed under the terms and conditions of the Creative Commons Attribution (CC BY) license.

1. Introduction

With the rapid exploitation of marine resources, austenitic 304 stainless steel has been widely applied for seawater pipelines, flanges, fasteners and sealing joints of offshore platforms [1–3], seawater desalination facilities and coastal infrastructures owing to its favorable formability, weldability and general corrosion resistance [4–7]. Nevertheless, assembly-induced narrow crevices are practically unavoidable for steel components [8]. Inside confined crevice spaces, consumption of dissolved oxygen, chloride enrichment and local acidification jointly initiate insidious crevice corrosion [9–11], which severely threatens structural safety and shortens the service lifetime of marine equipment [12]. For 304 stainless steel, whose corrosion resistance depends entirely on a thin, self-healing passive film, the occluded environment established inside a narrow gap is able to destabilize

the film even in ambient temperature seawater, so that crevice corrosion has become one of the most common causes of premature failure of marine stainless-steel components [11,12].

It must nevertheless be emphasized that 304 stainless steel is not, in general, recommended for continuous immersion in seawater. Because its pitting resistance equivalent number (PREN ≈ 18–19) is low compared with 316L or duplex grades, technical guidance from producers and published field experience commonly limit its continuous exposure to chloride-containing media to concentrations of the order of 200 mg/L Cl^- for certain service conditions, whereas seawater contains roughly 19,000 mg/L Cl^- [13,14]. The present study therefore does not advocate 304 stainless steel as a preferred material for long-term seawater immersion. Rather, it addresses the practical reality that a large amount of 304 equipment is already in service in coastal plants, in which unavoidable crevice geometries exist and replacement by more highly alloyed grades is not always economically feasible [6,12]. Under these circumstances, mitigation measures that can retard the crevice corrosion of existing 304 components are of genuine engineering value, although the intrinsic material limitation remains and must be acknowledged.

The evolution of crevice corrosion in chloride-containing seawater is generally described by an autocatalytic occlusion cell mechanism [9–11]. At the early stage, the oxygen inside the crevice is consumed faster than it can be replenished by diffusion, so that the crevice interior becomes an oxygen-depleted anodic region while the surrounding open surface remains cathodically active; the resulting oxygen concentration cell drives metal dissolution inside the gap. The confined geometry then traps the generated metal cations, whose hydrolysis lowers the local pH, and the excess positive charge attracts chloride ions that migrate into the crevice and accumulate. The combination of acidic, chloride-rich and oxygen-depleted conditions progressively destroys the passive film, sustains active dissolution and eventually leads to pitting-like attack deep inside the crevice. A key consequence of this mechanism is that the ohmic (IR) potential drop along the narrow, electrolyte-starved gap is large, which strongly limits the penetration of any externally applied protection signal into the crevice interior [10].

Traditional mitigation techniques exhibit intrinsic drawbacks for occluded crevice environments. Cathodic protection suffers severe IR voltage drop within narrow gaps, making it hard for the protective potential to propagate into crevice interiors [15]; higher polarization may further induce hydrogen embrittlement risk [16]. Organic coatings cannot fully fill micro-crevices [17], and coating delamination at crevice edges will introduce new corrosion risks [18]. Corrosion inhibitors are limited by poor mass transport efficiency inside confined crevices [19], resulting in unstable protective performance [20].

Anodic polarization protection stabilizes the electrode potential within the passive domain to promote passive film formation and self-repair [21], which is theoretically applicable to passivable alloys such as stainless steel. Anodic protection has been successfully implemented in concentrated acid medium industrial equipment [22,23], yet most existing anodic protection investigations focus on bulk solution conditions [24,25], rather than on complex occluded crevice scenarios in natural seawater [26,27]. If the applied potential exceeds the critical pitting or crevice corrosion potentials of the alloy in the seawater environment, anodic polarization can initiate or accelerate localized corrosion instead of protecting the metal [10,25]; therefore, the anode potential of anodic protection should be strictly controlled. Limited high-spatial-resolution in situ experimental evidence is available to reveal how anodic polarization modulates the potential/current distribution and passive film evolution inside seawater crevices [28,29].

In the present study, a 10 × 10 array electrode simulated crevice setup was adopted for static immersion experiments in natural Zhanjiang Bay seawater. In situ mapping of the galvanic potential and galvanic current, combined with EIS and surface morphology

characterization, was used to clarify the crevice corrosion evolution rule and the inhibition mechanism under intermittent anodic polarization. This work aims to provide fundamental experimental support for the crevice corrosion control of marine stainless-steel components.

2. Materials and Methods

2.1. Experimental Materials and Chemical Composition

Commercial 304 stainless steel wire was used in this work; its chemical composition (mass fraction) is shown in Table 1. The composition was provided in the mill certificate of the material and was verified by spark optical emission spectrometry in accordance with GB/T 11170-2008 [30] (equivalent to ASTM E1086 [31]).

Table 1. Chemical composition of as-received 304 stainless steel (wt. %).

Element	C	Si	Mn	P	S	Cr	Ni	N
Standard range	≤0.08	≤1.00	≤2.00	≤0.045	≤0.030	18.0–20.0	8.0–10.5	≤0.10
Measured value	0.05	0.50	1.20	0.030	0.015	18.5	8.3	0.03

Type 304 austenitic stainless steel was selected because it is one of the most widely used austenitic grades in the water systems of coastal power plants, and because its susceptibility to crevice corrosion in chloride media is well documented [4–7]. The material was supplied in the as-received, solution-annealed condition in the form of commercial wire with a diameter of 1.5 mm. As shown in Table 1, the chemical composition lies within the specification range for 304 stainless steel, with a chromium content of about 18.5 wt.% and a nickel content of about 8.3 wt.%, which provide the alloy with its passivation ability. The low carbon content (0.05 wt.%) limits sensitization during welding; in the present work, the wires were joined to the copper leads by a low-heat-input procedure followed by insulation, so that the metallurgical condition of the crevice-facing surface was essentially that of the as-received wire.

All microelectrodes used to construct the array were cut from the same wire batch in order to minimize compositional and microstructural scatter. The exposed working area of an individual microelectrode was approximately 1.77×10^{-2} cm^2 ($\Phi = 1.5$ mm), giving a total array working area of about 1.77 cm^2 distributed over the 10 × 10 grid.

2.2. Fabrication of the 10 × 10 Array Electrode and Assembly of the Simulated Crevice

Array electrodes were assembled from 304 stainless-steel wires ($\Phi = 1.5$ mm). Special care was taken to ensure that the array represented a continuous metal surface as faithfully as possible. The wires were arranged on a regular square grid and mounted in a mold such that their end faces were flush and coplanar, with the inter-wire gaps filled with epoxy resin to provide mechanical support and electrical insulation. Each steel wire was welded to copper lead wire, which allowed the electrochemical state of any single unit to be measured while the remaining units were either left at open circuit or connected together. Each microelectrode was insulated with 704 silicone rubber and embedded within epoxy resin molds to construct the 10 × 10 array electrode. Working surfaces were sequentially ground with 180#, 400#, 800#, and 1000# SiC abrasive papers, ultrasonically cleaned in anhydrous ethanol and acetone for 10 min each, then blow-dried using cold air. Electrical conduction and insulation performance for every microelectrode were individually checked to eliminate short-circuit and open-circuit defects.

Before assembly, the electrical integrity of the array was checked unit by unit in order to exclude short-circuit and open-circuit defects; only arrays in which all 100 microelectrodes

were confirmed to be electrically isolated from one another and reliably connected to their leads were used in the subsequent immersion tests (Figure 1).

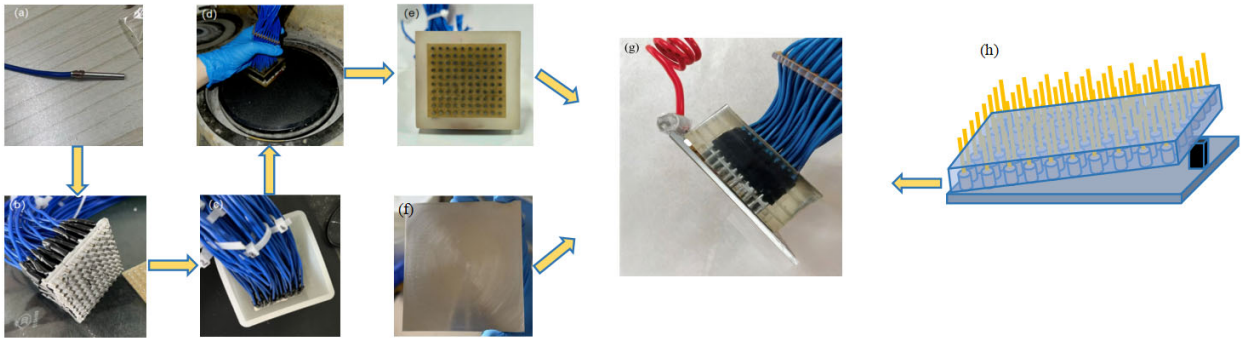


Figure 1. Fabrication procedure of the simulated crevice specimen based on a 10 × 10 array of 304 stainless-steel wires: (**a**) Microelectrode; (**b**) Assembly of the array electrode; (**c**) Encapsulation of the array electrode; (**d**) Polishing of the working surface of the array electrode; (**e**) Array electrode; (**f**) 304 stainless steel plate; (**g**) Simulated crevice specimen; (**h**) Schematic diagram of the simulated crevice specimen.

The simulated crevice assembly consisted of a 304 stainless-steel cover plate and the above array electrode. An ethylene–vinyl acetate (EVA) gasket with a thickness of 0.3 mm was inserted to precisely control the crevice gap width of 0.3 mm. The gap width of 0.3 mm was chosen because it lies within the range typical of engineering crevices formed by flange joints, gaskets and lap overlaps, and because a gap of this size is narrow enough to sustain oxygen depletion and chloride enrichment while remaining wide enough to avoid capillary blocking of the electrolyte. The cover plate and the array electrode were aligned and clamped together so that the EVA gasket defined a well-controlled crevice of uniform width over the entire array area. The gasket also sealed the crevice, so that mass exchange between the crevice interior and the bulk seawater took place only through the crevice mouth, reproducing the diffusion-limited conditions that prevail in real occluded joints. The crevice geometry was therefore defined by the gasket thickness (0.3 mm) rather than by the clamping force, which ensured that the gap width remained reproducible between specimens.

2.3. Seawater Characterization and Immersion Tests

The corrosive medium was natural seawater collected from Zhanjiang Bay (Zhanjiang, China), used without sterilization or artificial adjustment of its composition so that the tests reflected the natural water chemistry of the sampling site. The bulk seawater was characterized at the beginning of the exposure, and the main parameters are summarized in Table 2. The immersion temperature was 25 ± 2 °C (ambient). Seawater in the immersion tanks was fully renewed every seven days during the whole test period; because the dissolved oxygen concentration is one of the key variables controlling the oxygen concentration cell inside the crevice, the periodic renewal was also intended to keep the bulk oxygen level as stable as possible between measurements.

Two groups were set:

- Blank control group: Crevice specimens were immersed without external polarization, allowing spontaneous crevice corrosion evolution;
- Intermittent anodic polarization group: The whole array electrode served as the anode; a large-area 304 stainless-steel sheet acted as the counter electrode. An electrochemical workstation (CS350, CorrTest, Wuhan, China) executed the intermittent polarization protocol: an anodic potential of 0.1 V vs. SCE was applied for 10 min for every 30 min of free immersion period.

For each group, three independently assembled crevice cells were prepared and immersed simultaneously (n = 3). The galvanic potential/current maps and EIS spectra reported below are representative of the three specimens; the specimen-to-specimen scatter of the maximum galvanic potential difference was comparable to the temporal variation observed on a single specimen and was small compared with the difference between the blank and polarized groups.

Table 2. Characterization of the natural seawater (Zhanjiang Bay) used in this study.

Parameter	Value
pH	8.1 ± 0.1
Salinity	30.5 ± 0.5 ‰
Dissolved oxygen	6.2 ± 0.4 mg·L^{-1}
Chloride content	17.4 g·L^{-1}
Conductivity	45.6 mS·cm^{-1}
Temperature during exposure	25 ± 2 °C (ambient)
Exposure duration/renewal	75 d/full renewal every 7 d

2.4. Electrochemical Measurements and Surface Characterization

In situ galvanic potential and galvanic current distribution were acquired by the electrochemical noise module of the CS350 workstation. One microelectrode worked as working electrode W1; the remaining 99 microelectrodes were paralleled as W2 and acted as a large-area quasi-reference electrode. Microelectrode channels were switched sequentially to obtain galvanic signals between individual units. Origin 2026 software was adopted to plot 2D contour distribution maps. The galvanic potential of each unit was measured against the remaining 99 units connected in parallel, which form a quasi-reference electrode whose mixed potential is spatially averaged; the measured quantity is a relative potential distribution within the array, and the absolute value of the quasi-reference potential cancels when differences between units are compared. The potential resolution of the CS350 electrochemical noise module is 1 μV, and repeated scanning of the same channel within one mapping run differed by less than ±2 μV; the maximum differences reported (1.9–4.4 × 10^{-5} V) are therefore one order of magnitude above the measurement repeatability. The mapping at each immersion time was performed at a fixed time of day, and the water temperature during mapping was 25 ± 1 °C, so that the influence of diurnal temperature fluctuation on the small potential differences was limited.

Electrochemical impedance spectroscopy (EIS): Individual microelectrode units from the crevice interior toward the crevice mouth were sequentially tested. Distant microelectrodes were used as the counter electrode; an adjacent microelectrode served as the quasi-reference electrode. AC perturbation amplitude: 10 mV; frequency range: 100 kHz–10 mHz. EIS data were fitted using ZView 2.7 software. The EIS spectra were interpreted in terms of a simple film model (Rs(Qf‖Rf)) in which the solution resistance (Rs) is in series with a parallel combination of a constant-phase element (Qf), representing the non-ideal capacitance of the passive film, and a film resistance (Rf), representing the resistance to charge transport through the film. The impedance of the constant-phase element is given by $Z = 1/[Y(j\omega)^n]$, where Y is the admittance parameter, ω is the angular frequency and n is an exponent that reflects the deviation from ideal capacitive behavior; values of n close to unity indicate a compact, near-ideal film, whereas lower values indicate a more defective or porous film. The film resistance Rf is therefore a direct measure of the protective quality of the passive film, and its spatial variation along the crevice is an indicator of the local susceptibility to corrosion.

Morphology observation: A Leica DVM6 ultra-depth-of-field video microscope (Leica Microsystems, Wetzlar, Germany) was used to observe the micro-pitting morphology inside the crevices after 75 days of immersion. The pits on the crevice-facing surfaces were counted on the microscope images, and the pit density (pits per unit area), the mean pit diameter and the maximum pit depth were quantified.

3. Results

3.1. Galvanic Potential Distribution and Crevice Corrosion Evolution

For blank control crevice specimens immersed in natural seawater, the consumption of dissolved oxygen inside the confined gaps gradually establishes stable oxygen concentration cells as the immersion time increases. After 15 days of immersion, the galvanic potential presented an obvious band-shaped heterogeneous distribution parallel to the crevice extension direction. From the crevice depth toward the crevice mouth, the galvanic potential rose gradually, and the maximum galvanic potential difference continuously increased from 1.97×10^{-5} V (30 d) up to 4.38×10^{-5} V (75 d). Inside the crevice interior, metal cation hydrolysis induced a local pH drop, accompanied by Cl^- migration and enrichment, which destroyed the native passive films and accelerated local anodic activation, consistent with the classical crevice corrosion initiation theory for stainless steel in chloride-containing seawater [9–11]. The band-shaped potential distribution observed for the blank specimens is a direct manifestation of the occlusion cell mechanism. From the crevice mouth toward the interior, the progressive depletion of dissolved oxygen shifts the local open-circuit potential of the alloy in the active direction, so that the crevice interior becomes the anode of a macro-cell while the aerated mouth region acts as the cathode. The increase in the maximum potential difference from 1.97×10^{-5} V at 30 d to 4.38×10^{-5} V at 75 d shows that this macro-cell did not reach a steady state but continued to strengthen with the immersion time, which is consistent with the progressive accumulation of chloride and the continued acidification of the occluded electrolyte. The gradual strengthening of the potential heterogeneity also implies that the passive film inside the crevice was progressively degraded. As the local pH decreased and the chloride concentration increased, the film became thinner and more defective and the potential range over which it remained stable narrowed.

For the intermittent anodic polarization specimens (0.1 V vs. SCE, 10 min/30 min cycle), the original band-shaped potential zoning disappeared during the 15–75 d immersion (Figure 2b). The maximum galvanic potential difference was controlled below 1.93×10^{-5} V. Intermittent anodic polarization elevated the potential of the crevice inner regions, homogenized the spatial electrochemical heterogeneity, and promoted passive film regeneration and repair, suppressing the driving force for localized crevice corrosion. Different from continuous anodic protection, the intermittent mode reduces the total electric energy consumption and avoids the risk of overpassivation and transpassive dissolution. It should be emphasized that the suppression of the band-shaped potential zoning is not merely the result of a uniform shift in all local potentials in the same direction. The maximum galvanic potential difference, which is the driving force of the macro-cell, was reduced to below 1.93×10^{-5} V, a value smaller than that measured for the blank group even at an early stage of immersion. This indicates that intermittent anodic polarization acted by homogenizing the electrochemical state across the crevice, raising the potential of the most occluded regions toward the value of the aerated mouth region rather than polarizing the whole surface uniformly. Such homogenization removes the thermodynamic driving force of the macro-cell and, at the same time, keeps the local potential of the crevice interior within the passive domain, so that the passive film is stabilized instead of being driven into breakdown.

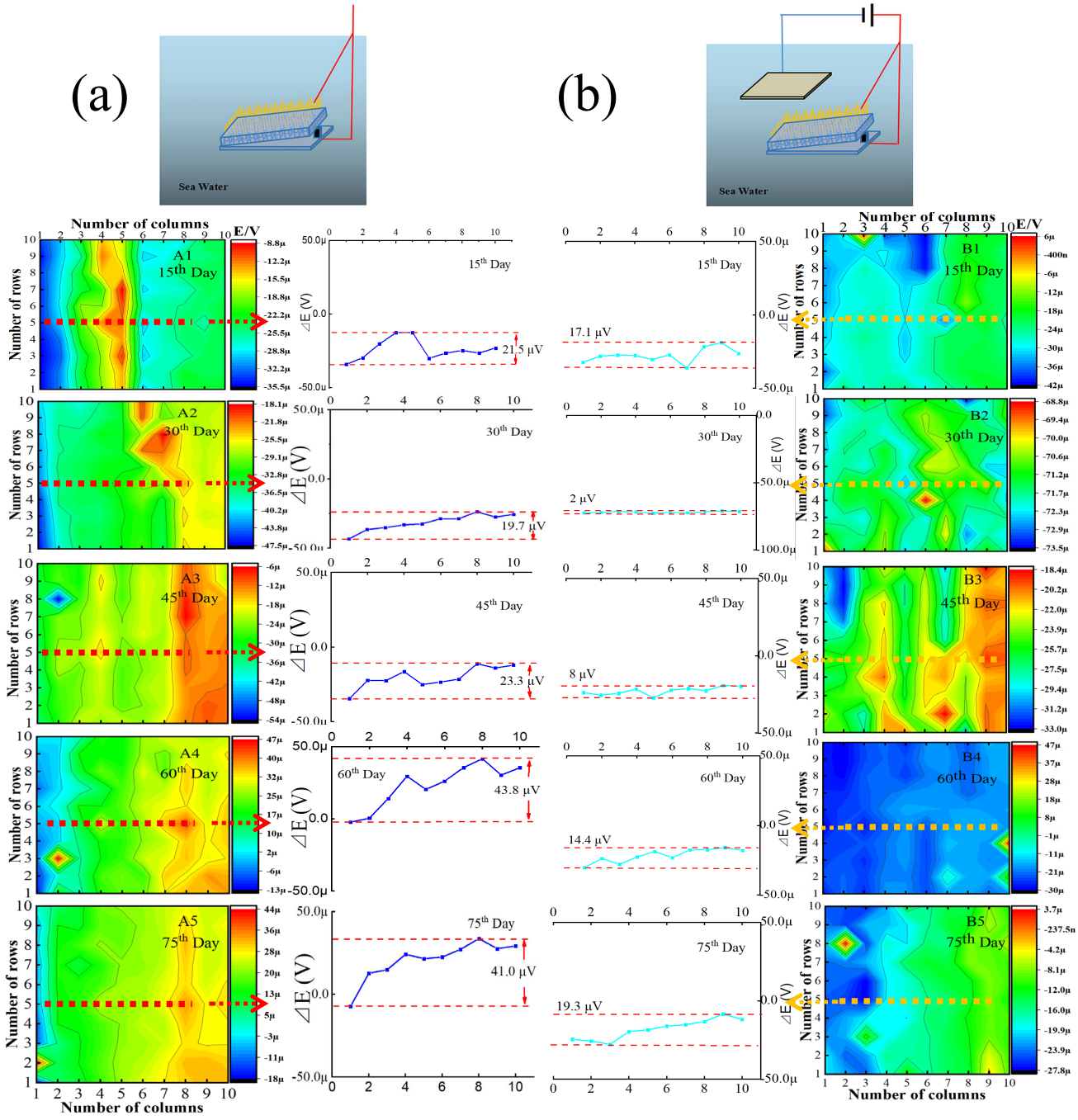


Figure 2. Two-dimensional contour maps of the galvanic potential distribution inside the simulated crevice of 304 stainless steel: (**a**) blank control group; (**b**) intermittent anodic polarization group, at different immersion durations.

3.2. Galvanic Current Distribution and Corrosion Morphology

In the blank group samples, the galvanic current exhibited a band-shaped distribution; the current amplitude grew with the immersion time, reflecting progressive aggravation of localized corrosion inside the crevice (Figure 3a). Under intermittent anodic polarization, the spatial distribution of the galvanic current became uniform, and the absolute magnitude of the galvanic current decreased significantly (Figure 3b).

The galvanic current maps provide a more direct measure of the localized corrosion intensity than the potential maps, because the current is proportional to the rate of the electrochemical reactions occurring at the electrode surface. In the blank group, the band-shaped current distribution and its increasing amplitude with the immersion time show

that both the spatial heterogeneity and the magnitude of the localized attack grew continuously; the highest current densities were consistently located in the crevice deep zones, in agreement with the potential maps and with the location of the pits observed after exposure. Under intermittent anodic polarization, both the spatial contrast and the absolute magnitude of the galvanic current were markedly reduced, indicating that the macro-cell current that sustained the propagation of crevice corrosion was effectively suppressed. The good correspondence between the potential and current maps confirms that the two independent in situ measurements consistently describe the same physical process.

After 75 days of static immersion, ultra-depth-of-field microscope observations demonstrated that the blank specimens possessed high-density pitting pits concentrated in the crevice deep zones (Figure 4A). In contrast, the number of pitting pits decreased substantially for the anodic polarization specimens (Figure 4B). To quantify these observations, the pits on the crevice-facing surfaces were counted and measured on the microscope images; the results are summarized in Table 3. The pit density of the polarized specimens was reduced to approximately one-seventh of that of the blank specimens, the maximum pit depth decreased from about 12 μm to about 4 μm, and the corroded area fraction decreased by roughly one order of magnitude. This morphological evidence macroscopically confirms that intermittent anodic polarization effectively suppresses the initiation of crevice corrosion pits within occluded crevices.

Table 3. Quantitative statistics of the pits observed inside the simulated crevice after 75 days of immersion.

Group	Pit Density (Pits·cm^{-2})	Mean Pit Diameter (μm)	Maximum Pit Depth (μm)	Corroded Area Fraction (%)
Blank control	43 ± 7	3.5	11.8	4.6
Anodic polarization	6 ± 3	2.2	4.1	0.7

The microscopic observations thus provide independent, post-mortem confirmation of the in situ electrochemical results. The reduction in both the number and the depth of pits inside the crevice is consistent with the interpretation that intermittent anodic polarization maintained the local potential within the passive domain and thereby prevented film breakdown, rather than merely slowing the growth of pits that had already initiated. It is also noteworthy that the protective effect was most pronounced in the deep region of the crevice, where the attack was most severe in the blank specimens; this spatial selectivity is a direct consequence of the fact that the polarization signal preferentially compensates the potential drop that develops in the most occluded region.

3.3. Passive Film State Evolution Inside the Crevice (EIS Analysis)

In the blank group, the film resistance increased monotonically from the crevice interior (2.62×10^6 Ω·cm^2) toward the crevice mouth (9.58×10^6 Ω·cm^2), whereas the admittance parameter Y was highest in the interior and lowest at the mouth (Table 4, Figure 5). This gradient directly reflects the spatial variation in the occluded environment: toward the interior, where oxygen is depleted, chloride is concentrated and the pH is lowest, the passive film was thinnest and most defective, so that its resistance was lowest and its capacitance highest. The relatively high n values (0.86–0.88) indicate that the films retained a predominantly capacitive character even in the most degraded region, which is consistent with a film that was locally thinned and defective rather than completely destroyed. Under intermittent anodic polarization, the passive films inside the crevice were repaired. The crevice inner film resistance Rf increased from 2.62×10^6 Ω·cm^2 to 2.59×10^7 Ω·cm^2. Meanwhile, the impedance differences among the different crevice positions were greatly reduced. Inter-

mittent anodic polarization regulates the metal–solution interfacial electrochemistry even within the mass transfer-limited occluded crevice, overcoming the *IR* drop bottleneck that plagues cathodic protection in narrow gaps.

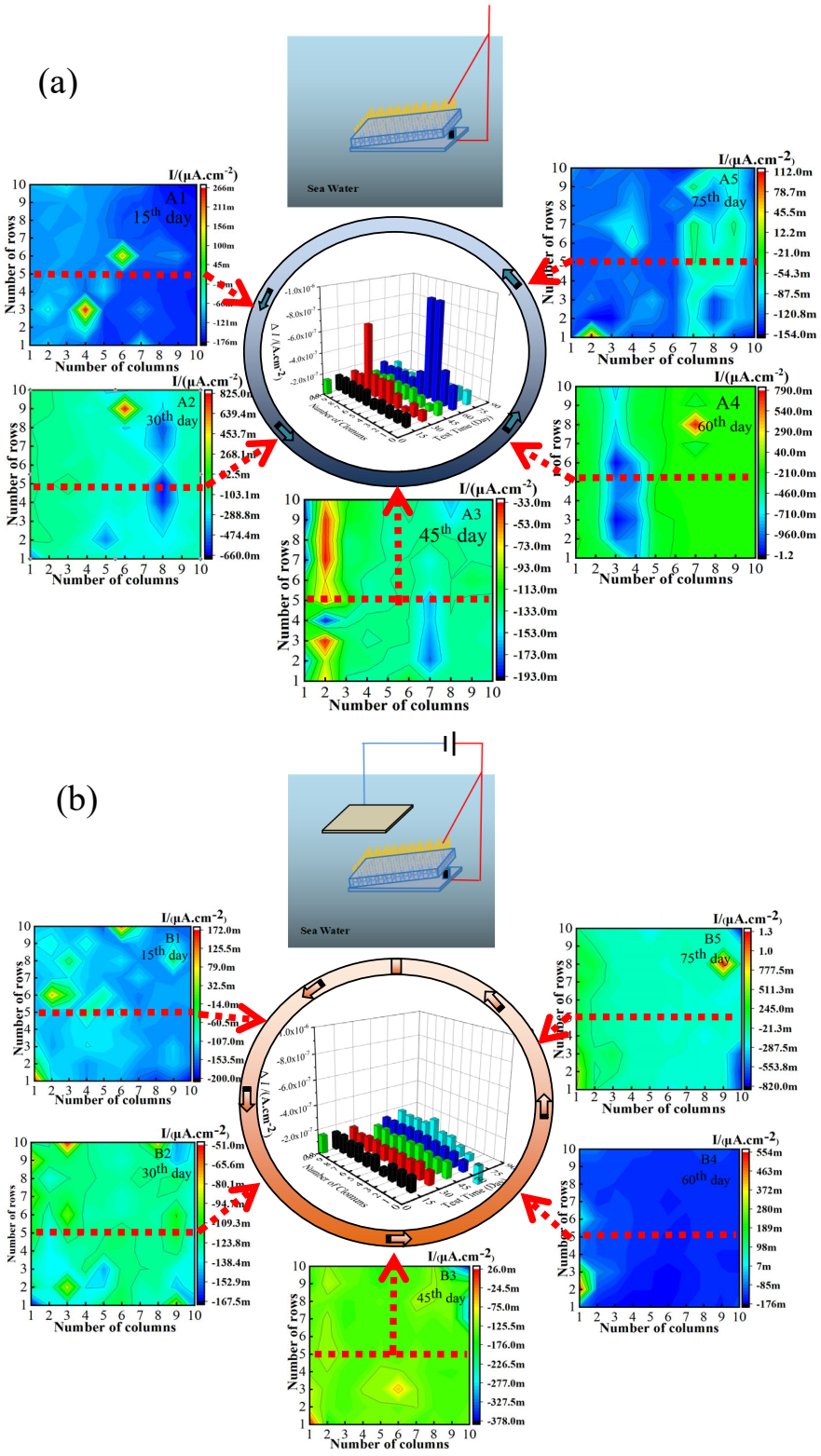


Figure 3. Two-dimensional contour maps of the galvanic current distribution inside the simulated crevice of 304 stainless steel: (**a**) blank control group; (**b**) intermittent anodic polarization group, at different immersion durations.

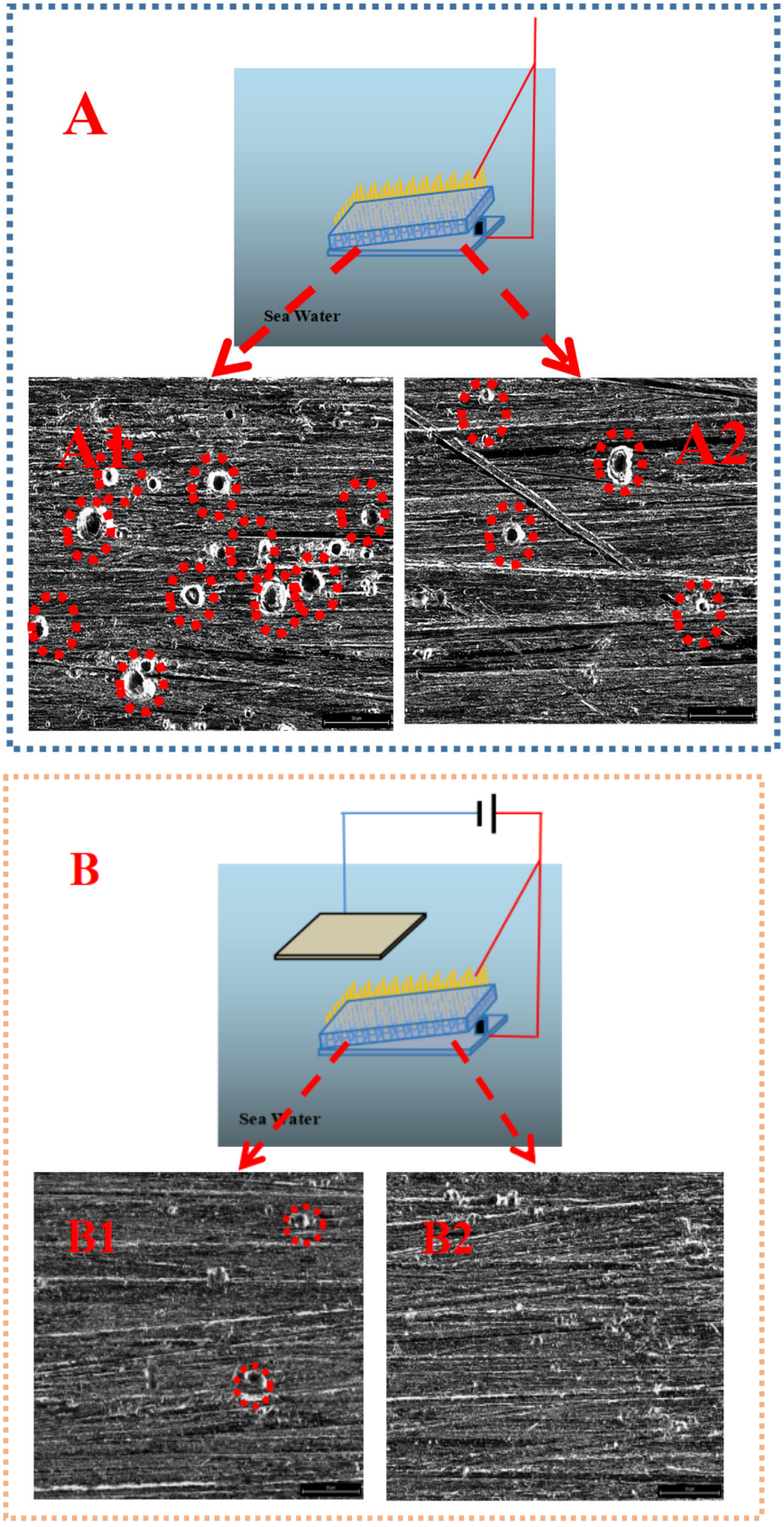


Figure 4. Comparison of the corrosion morphology inside the simulated crevice of 304 stainless steel: (**A**) blank control group ((**A1**) morphology in the deep crevice; (**A2**) morphology at the crevice opening); (**B**) intermittent anodic polarization group ((**B1**) morphology in the deep crevice; (**B2**) morphology at the crevice opening).

Table 4. Fitting parameters of the EIS equivalent circuit Rs(Qf‖Rf) at different positions inside the simulated crevice.

Group	Location	*Rs* ($\Omega \cdot cm^2$)	*Y* ($\Omega^{-1} \cdot cm^{-2} \cdot s^n$)	*n*	*Rf* ($\Omega \cdot cm^2$)
Blank control	Inner crevice	3.07	2.95×10^{-5}	0.86	2.62×10^6
	Middle crevice	4.58	2.99×10^{-5}	0.88	3.16×10^6
	Outer crevice	9.34	1.33×10^{-5}	0.88	9.58×10^6
Anodic polarization	Inner crevice	3.65	3.86×10^{-5}	0.83	2.59×10^7
	Middle crevice	4.89	3.03×10^{-5}	0.86	1.36×10^7
	Outer crevice	5.59	2.45×10^{-5}	0.88	2.49×10^6

A particularly informative feature of the treated specimens is that the spatial distribution of the film resistance was reversed with respect to the blank group: the highest *Rf* (2.59×10^7 $\Omega \cdot cm^2$) now occurred in the crevice interior and the lowest (2.49×10^6 $\Omega \cdot cm^2$) near the crevice mouth. In other words, intermittent anodic polarization preferentially strengthened the passive film in the most occluded and originally most vulnerable region. This reversal is a strong indication that the polarization signal was able to penetrate into the crevice interior and act directly on the metal/solution interface there, overcoming the IR drop limitation that restricts conventional cathodic protection in narrow gaps.

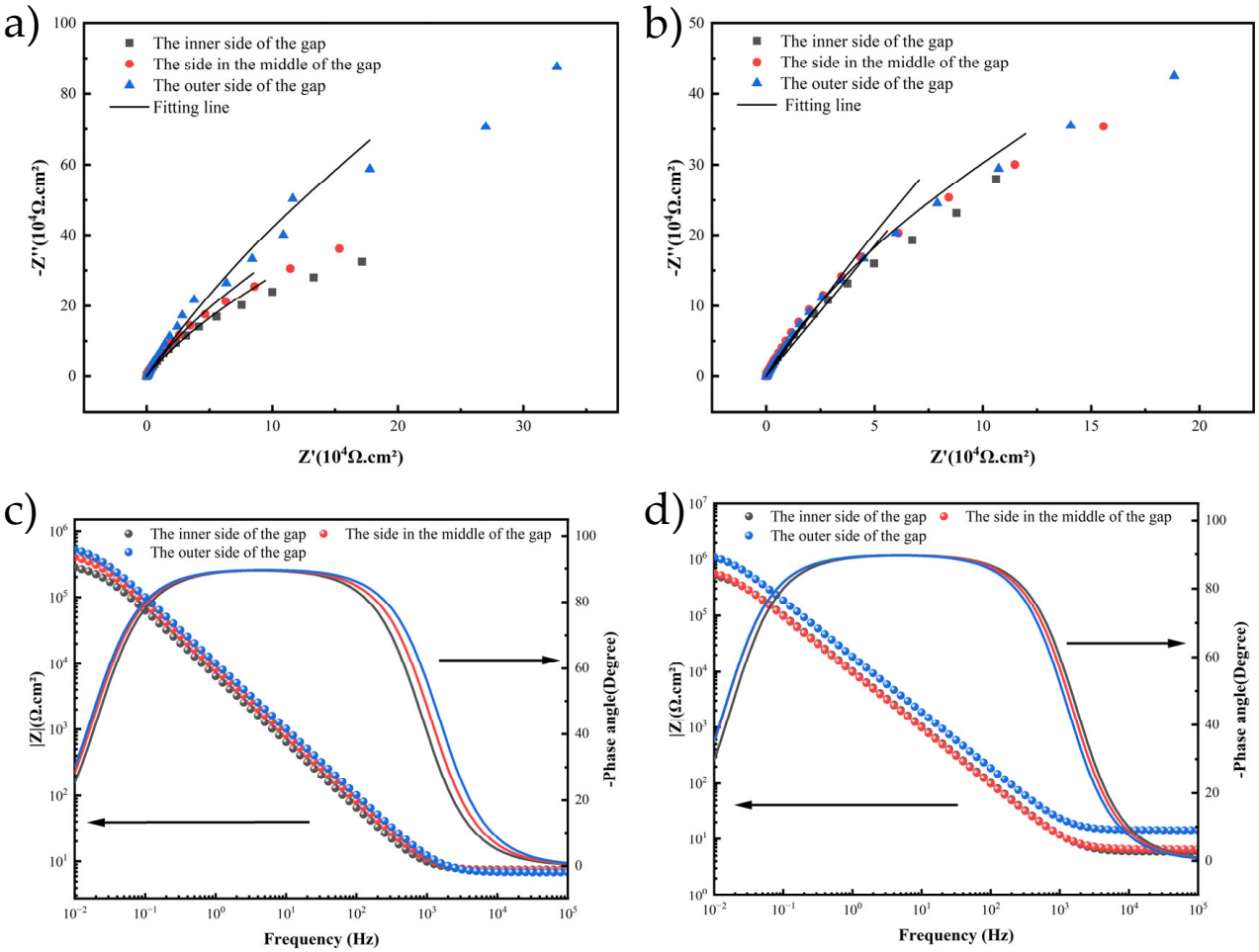


Figure 5. Electrochemical impedance spectra of the 304 stainless-steel crevice at the inner, middle and outer positions after 75 days of immersion: (**a**,**c**) blank control group; (**b**,**d**) intermittent anodic polarization group; (**a**,**b**) Nyquist plots; (**c**,**d**) Bode plots. The lines are the fitting results with the *Rs*(*Qf*‖*Rf*) circuit.

For the blank control crevice samples, oxygen depletion, chloride ion accumulation and local acidification destroyed the passive film within the crevice interior, resulting in a remarkable decrease in the interfacial charge transfer resistance, and a large impedance discrepancy existed between the crevice interior, middle zone and crevice mouth (Table 4). The slight increase in *Rs* in the treated specimens (from 3.07 to 3.65 $\Omega \cdot cm^2$ in the interior) further suggests that the ionic conductivity of the occluded electrolyte was somewhat modified, presumably because film repair reduced the release of metal cations into the crevice solution.

4. Discussion

4.1. Inhibition Mechanism of Intermittent Anodic Polarization

Combining the results presented above, the inhibition of crevice corrosion by intermittent anodic polarization can be described as a sequence of coupled electrochemical processes taking place inside the occluded cell. When the array electrode is polarized, the potential of every microelectrode unit, including those located deep inside the crevice, is driven toward the same value within the passive domain. Because the polarization is applied to the array as a whole, the potential difference between the crevice interior and the crevice mouth is reduced, and the oxygen concentration macro-cell that drives crevice corrosion is deprived of its driving force. The periodic polarization also promotes the repair of the passive film. During each polarization pulse, the raised interfacial potential accelerates the growth of a compact oxide film on the crevice surface, and the repaired film then limits the anodic dissolution of the substrate. The increase in the film resistance in the crevice interior by an order of magnitude, together with the decrease in the admittance parameter, confirms that the restored film was more compact and less defective than that of the blank specimens. Because film repair is most effective where the film was originally most degraded, the protection is automatically concentrated in the most vulnerable region of the crevice.

As a consequence of potential homogenization and film repair, both the macro-cell current and the local anodic current are suppressed, and the local chemical environment of the crevice is expected to evolve more slowly: the release of metal cations and the associated acidification are reduced, chloride enrichment is retarded, and the occluded environment therefore remains milder than in the blank specimens.

4.2. Comparison with Conventional Protection Strategies

Compared with cathodic protection, which is limited by the IR drop inside narrow crevices, intermittent anodic polarization directly adjusts the interfacial potential of the stainless-steel substrate to the passive potential domain, and mitigates crevice corrosion without hydrogen evolution risk. From an engineering standpoint, the results also highlight an important difference between intermittent and continuous anodic protection. Continuous polarization holds the whole surface at a constant potential, which tends to over-polarize the freely exposed region while remaining insufficient inside the crevice; in contrast, the intermittent regime allows the passive film to be repeatedly re-formed and then examined under natural immersion conditions, so that the protection is concentrated where it is most needed. The reduction in the total polarization time to one-third of the exposure period further lowers the energy consumption and the risk of hydrogen-related damage associated with sustained polarization, which are practical advantages for field application.

5. Conclusions

In the natural seawater occluded crevice of 304 stainless steel, an oxygen concentration cell gradually forms with immersion time. Oxygen consumption, chloride enrichment and local pH decline (inferred from the classical mechanism; not directly measured) jointly

damage the passive film. Galvanic potential and current show an obvious band-shaped heterogeneous distribution inside the crevice, and pitting preferentially nucleates in the crevice deep area.

Intermittent anodic polarization (0.1 V vs. SCE, 10 min every 30 min) homogenizes the potential distribution inside the crevice, reduces the maximum galvanic potential difference and suppresses the galvanic cell driving force for crevice corrosion. The selected potential remains below the critical localized corrosion potentials reported for 304 stainless steel in near-neutral chloride media, although these critical potentials were not directly determined in this study.

Intermittent anodic polarization realizes effective repair and regeneration of the passive film inside the crevice: the inner crevice film resistance increases by one order of magnitude and the quantitative pit density decreases to about one-seventh of that of the blank group. This method overcomes the mass transfer and IR drop limitations of traditional protection technologies for occluded crevices.

Intermittent anodic polarization is therefore proposed as a candidate supplementary protection strategy for existing stainless-steel components containing unavoidable occluded geometries in seawater service.

Author Contributions: Conceptualization, S.Y. and P.D.; methodology, G.W., G.Z. (Guanwen Zheng) and P.D.; formal analysis, S.Y. and P.D.; investigation, G.W.; writing—original draft preparation, G.W.; writing—review and editing, P.D.; supervision, G.Z. (Guo Zheng) and G.Z. (Guanwen Zheng); funding acquisition, G.Z. (Guo Zheng) All authors have read and agreed to the published version of the manuscript.

Funding: This research was funded by the Enterprise Technology Development Project of Guangdong Energy Group Co., Ltd. (Grant No. ZJP-PY-H2022-121).

Institutional Review Board Statement: Not applicable.

Data Availability Statement: The data presented in this study are available on request from the corresponding author.

Conflicts of Interest: Authors Guowei Wu, Guo Zheng and Guanwen Zheng are employed by Zhanjiang Power Co., Ltd. The remaining authors declare no conflicts of interest.

References

1. Wang, J.C.; Li, X.W.; Zheng, L.; Li, Y. Biofouling prevention and control technology for marine engineering equipment: From traditional methods to intelligent interface engineering. *Mar. Pollut. Bull.* **2025**, *223*, 118924. [CrossRef]
2. Du, F.M.; Mo, R.H.; Guo, Z.; Wang, J.; Yang, Y.; Zhang, S. Overview of wear-resistant coatings in marine environments. *J. Mar. Sci. Eng.* **2025**, *13*, 2121. [CrossRef]
3. Huang, C.; Zheng, W. Development of offshore engineering equipment and high-end shipbuilding industry: A case study of Dinghai District, Zhoushan, Ningbo. *J. Coast. Res.* **2020**, *104*, 700–704. [CrossRef]
4. Zhao, Y.H.; Jiang, Z.; Chen, R.F.; Tang, Z.; Sun, X.; Zhao, Z. Investigation of the corrosion stability of TiCN and diamond-like carbon (DLC) coatings on 304 stainless steel in simulated seawater: Electrochemical and numerical studies. *Int. J. Electrochem. Sci.* **2026**, *21*, 101295. [CrossRef]
5. Jelić, Z.G.; Martinović, I.; Pilić, Z. Inhibition of microbiologically influenced corrosion of 304 stainless steel by *Artemisia annua* L. in simulated seawater. *Alloys* **2025**, *4*, 20. [CrossRef]
6. Liu, X.H.; Zhang, H.X.; Tong, H.T.; Sui, Y.; Li, X.; Hou, J. Effect of surface roughness on the corrosion behavior of 304 stainless steel in seawater. *J. Mater. Eng. Perform.* **2024**, *34*, 18287–18297. [CrossRef]
7. Zu, W.H.; Pan, G.T.; Li, J.H.; Wang, S.; Zhang, G.; Liu, Y.; Liu, Y. Carbon nitride interlayer-enhanced TiO_2/WO_3 nanorods with surface oxygen vacancies for durable photocathodic performance on 304 stainless steel in simulated seawater. *Chem. Eng. J.* **2024**, *490*, 151533. [CrossRef]

8. Cao, A.G.; Yu, T.; Lu, Y.G.; Li, W. 17-4PH stainless steel fastener for high salt fog open-air marine coupling. *PLoS ONE* **2025**, *20*, e0336842. [CrossRef]
9. Hosseinpour, S.; Mameng, H.S.; Almen, M.; Liimatainen, M. Field exposure of duplex stainless steel in the marine environment: The impact of the exposure zone. *Corros. Mater. Degrad.* **2025**, *6*, 63. [CrossRef]
10. Nagaoka, A.; Yakuwa, H.; Yamamoto, R.; Amaya, K. Numerical analysis of stainless steel crevice corrosion initiation behavior with varying external potentials and initial crevice gaps. *J. Electrochem. Soc.* **2024**, *171*, 071502. [CrossRef]
11. Dai, N.W.; Leng, B.; Liu, H.J.; Dou, X.; Wang, J.; Yang, X.; Sun, H.; Li, X.; Huang, H. Unveiling crevice corrosion characteristic and mechanism of 347H stainless steel in high temperature molten solar salt environment. *Sol. Energy Mater. Sol. Cells* **2026**, *302*, 114331. [CrossRef]
12. Zhu, L.Y.; Dong, Z.H.; Cai, G.Y.; Li, Y.; Cui, Z. The effect of cold deformation on crevice corrosion and stress corrosion cracking behavior of 304 stainless steel. *Eng. Fail. Anal.* **2026**, *186*, 110515. [CrossRef]
13. Lee, Y.H.; Kim, Y.H.; Kim, H. Crevice corrosion resistance of stainless steels in natural sea water with different post welding treatment. *Corros. Sci. Technol.* **2003**, *2*, 219–224.
14. Mendoza Morales, D.; Cuevas Arteaga, C. Determination of the corrosion resistance of SS-304 in synthetic seawater at two temperatures using electrochemical noise and polarization curves. *Int. J. Electrochem. Sci.* **2016**, *11*, 8683–8696. [CrossRef]
15. Wang, K.X.; Song, B.L.; Wei, J.H.; Cao, W.; Zhang, L.; Zheng, H.; Li, W.; Redaelli, E.; Li, W. A review of the development of photoelectrochemical cathodic protection from the perspective of hole scavengers and interface synergy. *Chem. Eng. J.* **2025**, *521*, 167000. [CrossRef]
16. You, T.; Chen, L.P.; Wang, F.T.; Ma, D.H.; Wu, W.H. Cause analysis on corrosion of essential service water pipeline in coastal nuclear power plant. *Total Corros. Control* **2026**, *40*, 49–52.
17. Wu, Y.M.; Zhao, C.C.; Zhao, W.J. DL@Ti3C2Tx enhanced waterborne epoxy coating with superior active/passive anti-corrosion properties under 30 MPa hydrostatic pressure. *Corros. Commun.* **2025**, *20*, 1–12. [CrossRef]
18. Barbara, O.; Georg, M.; Bernhard, S.; Bognar, P.; Ngo, S.; Bretterbauer, K.; Paulik, C. Key parameters and mechanism of blistering of coil-coatings in humid-hot laboratory environments. *Prog. Org. Coat.* **2023**, *176*, 107373. [CrossRef]
19. Yang, W.; Tong, Y.B.; Yang, Y.; Ran, Q.; Dong, L. Preparation and corrosion inhibition performance of controlled-release ethyl cellulose@D-sodium gluconate microcapsules in simulated concrete pore solution. *Constr. Build. Mater.* **2026**, *506*, 145030. [CrossRef]
20. Liu, J.; Fu, Z.; Han, Z.; Wang, W.; Song, B.; Wei, J.; Cao, W.; Li, W. Data-driven prediction of crevice corrosion failure in stainless steel. *J. Mater. Eng. Perform.* **2026**, *35*, 39180–39193. [CrossRef]
21. Yu, Z.; Sun, Y.; Wu, H.; Guo, F.; Hu, J.; Liu, M.; Zhou, X.; Wu, H.; Hu, J.; Wang, L.; et al. Anodic protection enables moisture-stable $Mg_3(Sb,Bi)_2$ for thermoelectric cooling. *Nat. Mater.* **2026**, *25*, 1182–1189. [CrossRef]
22. Luo, S.; Song, Z.; Zheng, L.; Fan, J. Defect-dominated corrosion behavior and protection mechanism of an anodic iron oxide film fabricated in an aqueous electrolyte. *J. Mater. Sci.* **2026**, *61*, 3485–3500. [CrossRef]
23. Van Pham, H.; Kim, J.; Kwon, D.; Yang, C.; Shin, H.-C.; Moon, S. Comparative study on the formation efficiency of anodic oxide films on AA2024 in sulfuric acid and oxalic acid solutions. *Met. Mater. Int.* **2026**, *32*, 2407–2418. [CrossRef]
24. García Rueda, F.C.; Meléndez-González, P.C.; Torres-González, J.; Antaño-López, R.; Avalos-Elizondo, L.A.; López, H.; Manuel, J. Comparative study of annealed anodic films on iron, 1018 carbon steel, and 304L stainless steel: Morphological, compositional, electrochemical, and optical properties. *J. Mater. Sci.* **2025**, *60*, 17876–17899. [CrossRef]
25. Balusamy, T.; Mohan Sathyaraj, P.; Sivakumar, B.; Ravichandran, K.; Narayanan, T.S.N.S. Impact of plastic deformation on the passivation and transpassivation behaviour of AISI 304 stainless steel in acidic media. *J. Solid State Electrochem.* **2026**, *30*, 1767–1778. [CrossRef]
26. Buhari, J.; Said, N.S.M.; Kurniawan, S.B.; Changyan, H.; Pin, Y.S.; Eng, W.-T.; Hou, T.K.; Kumar, G.G.; Moi, P.S. A systematic review of anode surface chemistry, electron transfer mechanisms, and feasibility in wastewater microbial fuel cells. *Ionics* **2026**, *32*, 6687–6711. [CrossRef]
27. Ren, Y.; Wang, D.; Sun, S.; Li, Z.; Yao, Y.; Yang, Z.; Wang, H.; Song, J.; Yang, C.; Cai, Z.; et al. Dual-function surface engineering for enhancing anode stability in alkaline seawater oxidation. *Nat. Commun.* **2026**, *17*, 5178. [CrossRef]
28. Liu, C.; Tian, Y.; Khan, Z.A.; Meng, Y. Mitigation of tribocorrosion of metals in aqueous solutions by potential-enhanced adsorption of surfactants. *Friction* **2023**, *11*, 801–819. [CrossRef]
29. Amara, U.; Sarfraz, B.; Mahmood, K.; Mehran, M.T.; Muhammad, N.; Hayat, A.; Nawaz, M.H. Fabrication of ionic liquid stabilized MXene interface for electrochemical dopamine detection. *Microchim. Acta* **2022**, *189*, 64. [CrossRef]

30. *GB/T 11170-2008*; Stainless steel—Determination of multi-element contents-Spark discharge atomic emission spectrometric method (Routine method)[S]. Standards Press of China: Beijing, China, 2008.
31. *ASTM E1086-22*; Standard Test Method for Analysis of Austenitic Stainless Steel by Spark Atomic Emission Spectrometry[S]. ASTM International: West Conshohocken, PA, USA, 2022.

Disclaimer/Publisher's Note: The statements, opinions and data contained in all publications are solely those of the individual author(s) and contributor(s) and not of MDPI and/or the editor(s). MDPI and/or the editor(s) disclaim responsibility for any injury to people or property resulting from any ideas, methods, instructions or products referred to in the content.